(Received 12 February 2026, Accepted 5 March 2026, Scheduled 17 April 2026)

Design and Analysis of a Flux Modulated Hybrid Excitation Linear Machine for Long Stroke Applications

Liang Xu*, Lei Zhao, and Tingting Jiang

School of Electrical and Information Engineering, Jiangsu University, Zhenjiang 212013, China

ABSTRACT: A hybrid excitation linear machine with all excitations on the primary has the advantage of low cost in long-stroke applications and flexible flux regulation. The permanent magnet and field winding concurrently contribute to the effective thrust force, that is, the permanent magnet excitation thrust force and electrical excitation thrust force. However, the insufficient utilization of the two magnetic fields limits the thrust force enhancement. To enhance the thrust force, this study proposes a flux-modulated hybrid excitation linear machine with improved concurrent utilization of air-gap magnetic fields from permanent magnets and field windings. First, the topology and operating principle of the machine are interpreted. An analytical model was built to analyze the air-gap magnetic field harmonics and flux linkage from the permanent magnet and field winding. In addition, the electromagnetic performance, including the flux regulation capability and thrust force, was investigated using finite element analysis. It was found that its average thrust force and flux regulation capability were significantly improved compared with the counterpart.

1. INTRODUCTION

Linear motion is the most common motion mode in industrial applications, and the performance optimization of its drive system has always been a research focus [1]. Permanent magnet linear machines (PMLM) have been widely adopted in direct-drive applications such as computer numerical control machine tools, electromagnetic launch technology, and new energy vehicles, owing to their advantages of high force density, high precision and high reliability [2, 3].

In conventional PMLM, armature winding and permanent magnet (PM) are typically separated into primary and secondary components, requiring full-length PM placement along the entire travel range. This leads to a significant increase in the consumption of rare-earth materials and higher costs for long-stroke applications. To address this issue, a novel primary-excited PMLM (PE-PMLM) that integrates both PM and armature windings into a short primary while employing a salient long secondary structure is proposed. This design maintains a high force density while drastically reducing PM usage, offering a cost-effective approach. Research indicates that such machines exhibit significant cost advantages compared with the traditional PMLM used in long-stroke scenarios, such as ropeless elevators, logistics transport systems, and urban rail transit [4, 5].

Based on PM arrangement, PE-PMLM can be further categorized into three topological structures: flux switching PMLM (FS-PMLM), flux reversal PMLM (FR-PMLM), and vernier PMLM (VPMLM). FS-PMLM is proposed by Zhu et al., which achieves flux switching through segmented PMs [6]. These machines show promising applications in rail transit and electromagnetic launch systems [7, 8]. Although cogging force suppression has been studied in FS-PMLM [9], it still faces challenges such as significant force ripple and low PM utilization. FR-PMLM is initially applied in single-phase linear oscillatory motors [10]. With PMs mounted on primary tooth surfaces, a simpler and more reliable structure than FS-PMLM is demonstrated, along with higher robustness [11]. VPMLM shares similar robustness with FR-PMLM. And by high pole-pair design, it achieves superior magnetic transmission. Compared to the previous two types, VPMLM demonstrates higher force density [12]. Recent studies have improved electromagnetic performance through flux concentrating structure optimization and fractional-slot design [13, 14]. With its low-speed high-force characteristics, VPMLM has become an important research direction in linear drive systems.

The three main types of PE-PMLMs demonstrate notable cost advantages in long-stroke applications. However, their flux regulation relies solely on the d-axis current, which risks irreversible demagnetization and offers a limited adjustment range. By introducing an additional separated field winding, various types of hybrid excitation linear machines can be derived from PE-PMLMs, which inherit the low cost for long-stroke applications and offer flexible flux regulation capability by utilizing field windings [13]. It is also shown that these machines derived from the PE-PMLMs are operated based on flux modulation principle, thus they are termed as flux-modulated hybrid excitation linear machines (FM-HELMs).

As regards FM-HELMs for long-stroke applications, their primaries are considerably congested because all the excitation sources, including armature windings, field windings, and PMs are located on the primary, which reduces the thrust force [14]. Recently, an integrated winding technique, which was first proposed for a variable flux reluctance machine drive, was devel-

* Corresponding author: Liang Xu (xuliang0511@ujs.edu.cn).

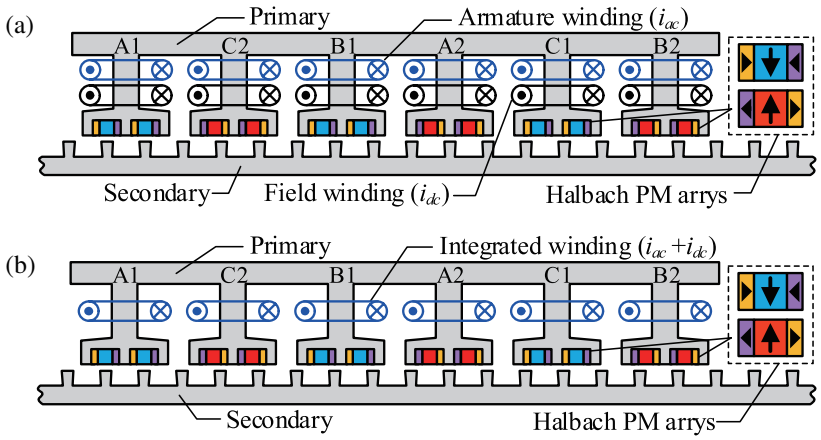

FIGURE 1. Topology of FM-HELM. (a) Separated winding. (b) Integrated winding.

oped and employed for FM-HELMs [15]. For HELMs adopting the integrated winding technique, the armature and field windings can be integrated into one set of windings with a dc-biased sinusoidal current. Thus, the spatial conflict between the armature and field windings can be eliminated, which reduces the copper loss to improve the thrust force output and expand the flux regulation capability. In [16], an integrated winding FM-HELM with slot PM was proposed. The thrust force was improved with the integrated winding, whereas the PM utilization was low because the horizontally magnetized PM flux almost did not pass through the air gap. In [17], vertical magnetization PM was employed in the FM-HELM. The PM flux leakage was relieved, and the thrust force was improved. As a flux-modulated machine that operates based on the air-gap magnetic field harmonic, the efficient utilization of the air-gap magnetic field harmonics generated by both PM and field winding excitations remains a challenging obstacle that restricts the thrust force FM-HELMs [18].

To improve the thrust force density, this study proposes an FM-HELM featuring improved concurrent utilization of the two magnetic fields. The inset PM array mounted on the tooth surface is designed to have the same pole pair as that of the field winding, which allows efficient utilization of air-gap magnetic fields from the PM and excitation current (EC). Meanwhile, the introduction of EC not only generates electrical excitation thrust force but also relieves direct current (DC) magnetic saturation in primary iron core. The remainder of this paper is organized as follows. Section 2 describes the machine topology and operation principle. Section 3 elucidates thrust force enhancement by calculating the air-gap magnetic field and analyzing the relief of dc magnetic saturation in the primary iron core. The electromagnetic performance analysis and comparison are presented in Section 4. Finally, Section 5 provides the concluding remarks.

2. MACHINE TOPOLOGY AND OPERATION PRINCIPLE

2.1. Machine Topologies

The machine topologies of the 6-primary-teeth and 17-secondary-teeth FM-HELM with separated and integrated windings are illustrated in Fig. 1. The two machines share the same topology, except for the winding schemes. Fig. 1(a) shows the FM-HELM with separated windings, which suffers from a spatial conflict between the armature and field windings. Fig. 1(b) shows an integrated winding configuration that combines the armature with field windings into a unified structure, thereby eliminating spatial conflict.

In the FM-HELM, each primary tooth shoe is notched with two auxiliary slots, thereby forming three split-teeth. The auxiliary slots are embedded with Halbach PM arrays, featuring flux-concentrating effects. Each Halbach PM array consisted of three PMs with different magnetization directions, that is, one piece of vertically magnetized PM in the center and two pieces of horizontally magnetized PMs on both sides. This unique arrangement enhances the magnetic field strength in the vertical direction of the device. Two identical Halbach PM arrays were placed under each primary tooth, forming one PM elementary unit. Adjacent primary teeth are equipped with one PM elementary unit of opposite polarity. The PM flux forms closed loops between adjacent primary teeth, resulting in a PM field with three pole pairs.

The EC should form a magnetic field with the same three pole pairs to cooperate with the PM field. Therefore, the field winding in the FM-HELM with a separated winding is fed with a DC current having an alternating direction between adjacent slots (see Fig. 1(a)). Furthermore, because the armature and field windings have the same wound direction on every tooth, the two types of windings can be merged into an integrated winding with the appropriate DC current direction, as shown in Fig. 1(b). By comparing Figs. 1(a) and 1(b), it can be observed that the same magnetic field produced by the EC can be built, verifying the effectiveness of the integrated winding.

The pole-slot combinations of the proposed FM-HELM satisfies the following relationship

$$\begin{cases} N_p = 2mk \\ N_s = nN_p \pm j \end{cases} \tag{1}$$

where N_p and N_s are primary and secondary teeth numbers; m is the phase number; n is the number of split-teeth of each primary tooth; k and j are positive integers.

In this study, three-phase winding and six primary teeth are adopted, i.e., $m = 3$ and $k = 2$. Also, to achieve a high pole ratio and high thrust force density, N_s should be close to the total number of primary split-teeth, so j is taken as 1 or 2.

By comparing FM-HELM models for $n = 2$, 3, and 4 using finite element analysis (FEA), the FM-HELM with n, j, and N_s, being 3, 1, and 17 offers the best thrust force performance. Then, it is ultimately selected for in-depth study.

2.2. Operation Principle

Figure 2 depicts the flux distribution at typical secondary positions within one electrical cycle under the flux-enhancing ($+I_{dc}$) condition. The green lines represent the EC flux entering the air gap through the split-teeth, and the blue lines represent the PM flux entering the air gap. The split-teeth configuration yields parallel flux circuit integration of the PM and EC fluxes. In addition, it effectively blocks the direct penetration of EC flux through PMs, thereby significantly mitigating the risk of irreversible demagnetization of PMs.

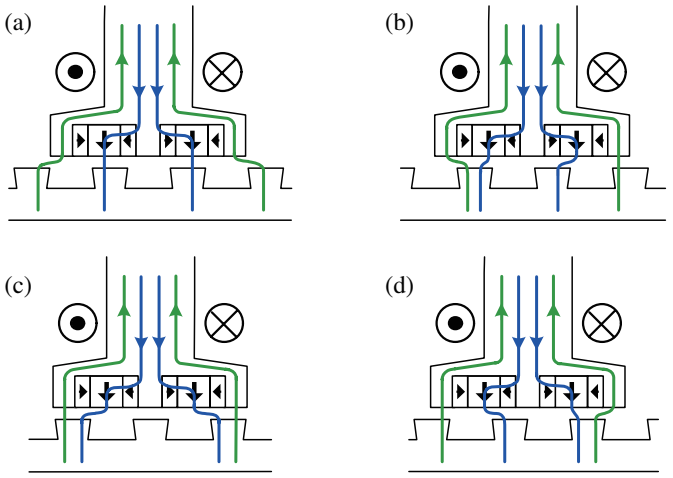

FIGURE 2. Schematic flux distribution excited by PM and EC ($+I_{dc}$). (a) The a position. (b) The b position. (c) The c position. (d) The d position.

As illustrated in Fig. 2, the directions of both EC flux and PM flux remained constant during the secondary movement, although they opposed each other. Consequently, the flux linkages generated by the PM (ψ_m) and EC (ψ_e) exhibit unipolar characteristics with opposite polarities.

Figure 3 presents the waveforms of the open-circuit flux linkage and back electromotive force (back-EMF) during one electrical cycle under PM, EC, and hybrid excitation conditions, where the labeled positions (a)–(d) correspond to those in Fig. 2. The direction of the flux from the air gap to the primary winding is defined as positive, which aligns with the EC flux shown in Fig. 2. The following analysis elaborates on the flux, flux linkage, and back-EMF characteristics at these four critical positions.

When the secondary core is at position a, the PM arrays align with the secondary teeth, resulting in the maximum permeance of the PM flux circuit (Λ_m). This causes the PM flux linkage to reach its negative maximum. Simultaneously, the split-teeth align with the secondary slots, leading to the minimum permeance of the EC flux circuit (Λ_e), which causes the EC flux linkage to reach its positive minimum. For the quarter electrical cycle in the case of the secondary movement from position a to position b, the magnitude of PM flux linkages reduces with decreases of Λ_m. Also, the EC flux linkage increases with the increase of Λ_e. At position c, it presents an inverse scenario compared to position a, namely, the PM arrays align with the secondary slots while the split-teeth coincide with the secondary teeth. Under this condition, Λ_m reaches its minimum whereas Λ_e attains its maximum. This results in the PM flux linkage achieving its negative minimum and the EC flux linkage achieving its positive maximum. In another quarter electrical cycle, the secondary core moves from position c to position d. The magnitude of PM flux linkages increases with the increase of Λ_m. Also, the EC flux linkage decreases with the decrease of Λ_e.

By analyzing the variations in permeance and flux, the trend in flux linkage was deduced, as shown in Fig. 3(a). Although the PM and EC flux linkages have opposite polarities, their phases are aligned. The introduction of the EC increases the ac component of the flux linkage while reducing its dc component. The reduction in the dc component relieves primary iron core saturation to improve iron core utilization. Furthermore, because the flux linkages of the PM and EC share the same phase, their induced back-EMFs are also in phase, thereby improving the thrust force and flux regulation capability.

When the integrated winding is fed with an opposite directional DC current, the polarity of the EC is reversed, and the EC flux linkage undergoes a 180° phase shift relative to the PM flux linkage. The ac component of the resultant flux linkage diminishes, leading to a reduction in the back-EMF. Evidently, bidirectional flux linkage regulation can be realized by adjusting both the polarity and magnitude of the EC.

3. ANALYTICAL MODELING AND ANALYSIS

In the proposed FM-HELM, the PM and EC work synergistically and jointly generate an electromagnetic thrust force that conforms to the flux modulation theory. To further reveal its intrinsic operating mechanism, analytical calculations are conducted based on the magnetomotive force (MMF) permeance model. In addition, the flux density and flux linkage can be analyzed based on this.

3.1. Permeance Function

Owing to the dual-salient structure, the slotting effects of both the primary and secondary sides must be considered. The conformal transformation method can be employed when calculating the permeance functions for the primary and secondary.

Because the widths of the primary virtual slots, split-teeth, and slot openings are inconsistent, the primary permeance function λ_p can be divided into two parts: the slot opening permeance function λ_{ps} and the virtual slots permeance function λ_{pm}.

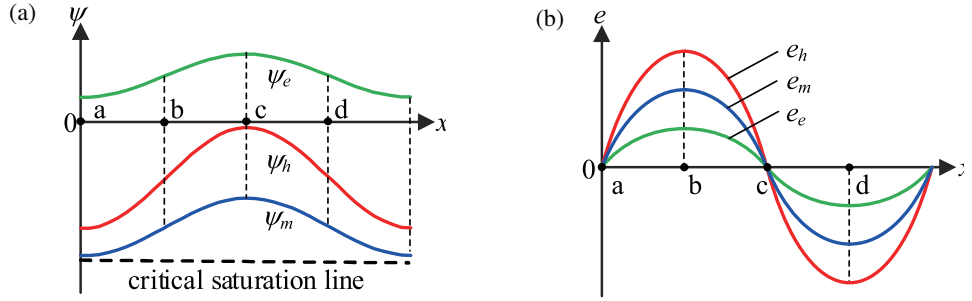

FIGURE 3. Open circuit flux linkage and back-EMF within one electrical cycle under different excitation conditions. (a) Flux linkage. (b) Back-EMF.

Thus, λ_p can be expressed as

$$\begin{cases} \lambda_p(x) = \lambda_{ps}(x) \cdot \lambda_{pm}(x) \\ \lambda_{ps}(x) = \lambda_{ps,0} - \sum\limits_{h=1}^{\infty} \lambda_{ps,h} \cos\left(\frac{2h\pi N_p}{L_0} x\right) \\ \lambda_{pm}(x) = \left[\lambda_{pm,0} - \sum\limits_{l_1=1}^{\infty} \lambda_{pm,l_1} \cos\frac{2l_1\pi N_p(x+x^*)}{L_0}\right] \\ \cdot \left[\lambda_{pm,0} - \sum\limits_{l_2=1}^{\infty} \lambda_{pm,l_2} \cos\frac{2l_2\pi N_p(x-x^*)}{L_0}\right] \end{cases} \quad (2)$$

where N_p is the number of primary teeth; L_0 is the total length of the primary; and x^* is the relative displacement between the primary auxiliary slot and the center of the primary tooth. Where $\lambda_{ps,0}$, $\lambda_{ps,h}$, $\lambda_{pm,0}$ and $\lambda_{pm,l1}$, $\lambda_{pm,l2}$ are the primary permeance coefficients. A schematic diagram of the primary permeance function is shown in Fig. 4.

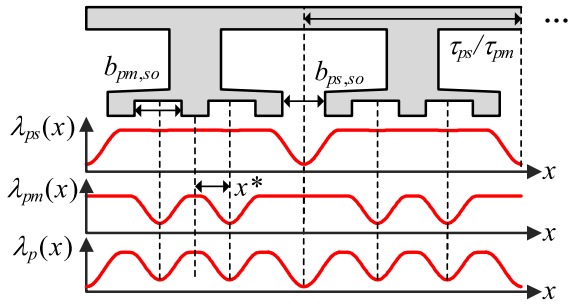

FIGURE 4. Primary permeance function.

The secondary core undergoes translational motion, and its permeance function λ_s can be expressed as

$$\lambda_s(x,t) = \lambda_{s,0} - \sum_{j=1}^{\infty} \lambda_{s,j} \cos\frac{2j\pi N_s(x+vt-x_{s0})}{L_0} \quad (3)$$

where N_s is the effective number of secondary teeth; $x_{s,0}$ is the secondary initial position; v is the translational velocity; $\lambda_{s,0}$ and $\lambda_{s,j}$ are the permeance coefficients. A schematic of the secondary permeance function is shown in Fig. 5.

The permeance coefficient can be calculated as

$$\begin{cases} \lambda_{x,0} = 1 - 1.6\beta\varepsilon \\ \lambda_{x,w} = \frac{4\beta}{w\pi}\left[0.5 + \frac{(w\varepsilon)^2}{0.78-2(w\varepsilon)^2}\right]\sin(1.6w\pi\varepsilon)^2, w = 1,2,\ldots \\ \beta = 0.5 - \frac{0.5}{\sqrt{1+(0.5b_{x,so}/g)^2}}, \varepsilon = \frac{b_{x,so}}{\tau_x} \\ x = ps,\ pm,\ s \end{cases} \quad (4)$$

where $b_{x,so}$ is the slot opening width, and τ_x is the length of the corresponding pole pitch.

3.2. MMF

For the FM-HELM, each primary tooth is equipped with two Halbach PM arrays. The two Halbach PM arrays in conjunction with the other two Halbach PM arrays in the adjacent primary tooth form two independent magnetic circuits as shown in Fig. 6(a). As shown, the flux of each magnetic circuit starts from a Halbach PM array and passes successively through the air gap, secondary iron core, air gap, oppositely polarized Halbach PM array, primary iron core, and finally returns to the originating Halbach PM array.

Because the two magnetic circuits are identical, it is sufficient to analyze only one closed magnetic circuit. The MMF generated by the Halbach PM array can be regarded as the superposition of the MMFs produced individually by the vertically magnetized PMs and horizontally magnetized PMs. Based on this, ideal equivalent MMF models for vertically and horizontally magnetized PMs were established, as illustrated in Figs. 6(b) and 6(c), respectively.

Based on simplified magnetic circuits and the equivalent MMF model, the MMF generated by the vertically magnetized PM (F_{g1}) and horizontally magnetized PM (F_{g2}) amplitudes can be calculated as

$$\begin{cases} F_{g1} = \frac{2B_r w_1 w_2 g}{\mu_0(gh_{pm}^2 + 2w_1 w_2 h_{pm} + 2\mu_r g w_1 w_2)} \\ F_{g2} = \frac{2B_r w_1 w_2 h_{pm} g}{\mu_0(2gw_2 h_{pm} + 2\mu_r g w_1 h_{pm} + 2w_1^2 w_2 + \mu_r w_1^3)} \end{cases} \quad (5)$$

where h_{pm} is the height of the PM; w_1 is the width of the vertically magnetized PM; w_2 is the width of the horizontally magnetized PM; B_r and μ_r are the remanence and relative permeability of the PM, respectively; g is the thickness of the air gap; and μ_0 is the vacuum permeability.

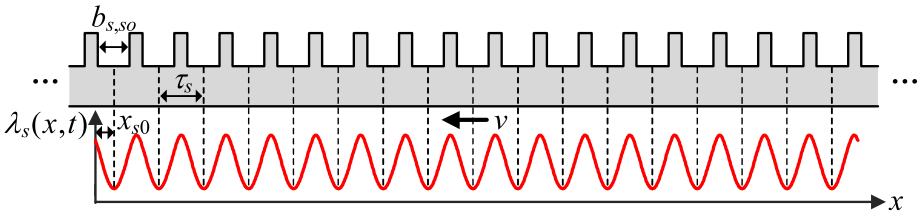

FIGURE 5. Secondary permeance function.

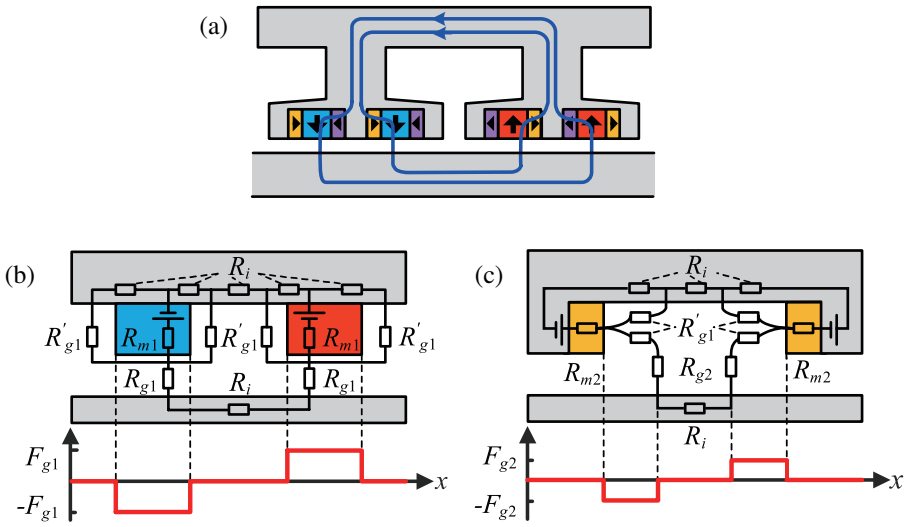

FIGURE 6. Simplified magnetic circuits and equivalent MMF models. (a) Simplified magnetic circuits. (b) MMF model of vertically magnetized PM array. (c) MMF model of horizontally magnetized PM array.

Based on (4), the MMF produced by the Halbach PM array can be expressed as

$$\begin{cases} F_m(x) = \sum\limits_{i=1,3\ldots}^{\infty} F_{m,i} \sin(\frac{2i\pi P_m}{L_0} x) \\ F_{m,i} = \frac{8(F_{g1}+F_{g2})}{i\pi}(-1)^{\frac{i+1}{2}} \sin\frac{i\pi P_m w_1}{L_0} \\ \qquad \cos\frac{i\pi P_m(w_3+2w_2+w_1)}{L_0} \end{cases} \tag{6}$$

where P_m is the number of pole pairs in the PM field, and w_3 is the width of the primary split-teeth.

The EC MMF is related to the number of turns in the integrated winding and the amplitude of the EC. The EC MMF can be expressed as follows:

$$\begin{cases} F_e(x) = \sum\limits_{k=1,3\ldots}^{\infty} F_{e,k} \sin(\frac{2k\pi P_e}{L_0} x) \\ F_{e,k} = \frac{4N_c \cdot I_{dc}}{k\pi} \end{cases} \tag{7}$$

where P_e is the number of pole pairs of the EC field; N_c is the number of turns in the integrated winding; and I_{dc} is the root-mean-square value of the DC current component in the integrated winding.

3.3. The Air-Gap Flux Density

The PM MMF calculation incorporates the primary permeance function. Considering the modulation effect of the secondary permeance function on the PM MMF, the air-gap flux density under PM excitation can be expressed as

$$B_m(x,t) = \frac{\mu_0}{g} F_m(x) \lambda_s(x,t) \tag{8}$$

By multiplying the EC MMF and primary and secondary permeance functions, the air-gap flux density under EC excitation can be expressed as

$$B_e(x,t) = \frac{\mu_0}{g} F_e(x) \lambda_p(x) \cdot \lambda_s(x,t) \tag{9}$$

Table 1 lists the air-gap flux density harmonics under PM and EC excitations. The air-gap flux density harmonics in groups 1–3 were produced by PM excitation, and those in groups 4–6 were produced by EC excitation. The harmonics in groups 1 and 4 are stationary, which are produced from the MMF modulated by 0-order harmonic of the secondary permeance function. The harmonics in the other groups are moving, produced by the MMF modulated by j-order harmonics of the secondary permeance function.

Figures 7 and 8 depict the comparison of the air-gap flux density under PM and EC excitations by analytical and FEA calculation. It can be seen that the waveforms and harmonics calculated by analytical and FEA are in good agreement. The major harmonics are labeled in Figs. 7(b) and 8(b). As shown, the major harmonic orders are also consistent with the results

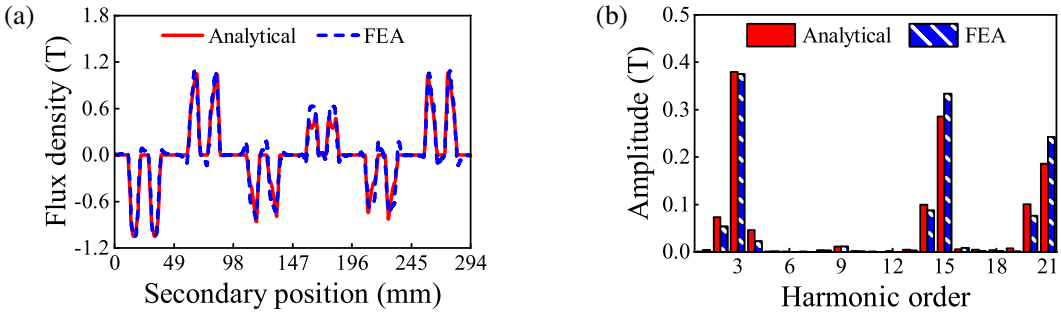

FIGURE 7. The air-gap flux density under PM excitation. (a) Waveforms. (b) Harmonics.

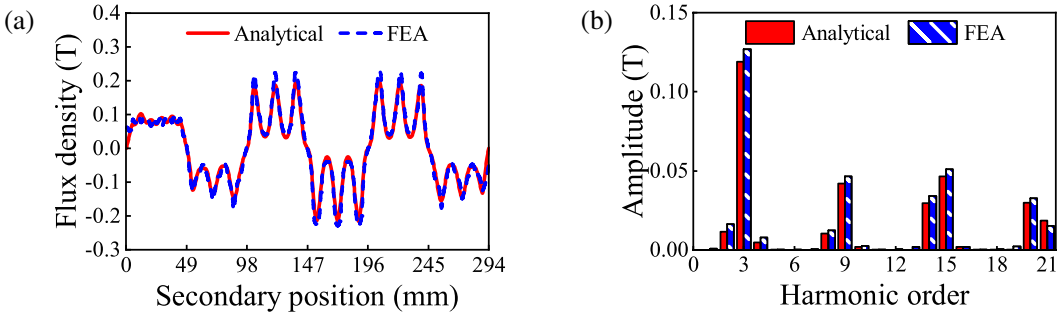

FIGURE 8. The air-gap flux density under EC excitation. (a) Waveforms. (b) Harmonics.

TABLE 1. The air gap flux density harmonic characteristic.

Group	Harmonic combination	Harmonic order	Velocity
1	$(i, 0)$	iP_m	0
2	(i, j)	iP_m+jN_s	$vjN_s/(iP_m+jN_s)$
3	(i, j)	$\|iP_m-jN_s\|$	$vjN_s/(iP_m-jN_s)$
4	$(k, 0)$	kP_e	0
5	(k, j)	kP_e+jN_s	$vjN_s/(kP_e+jN_s)$
6	(k, j)	$\|kP_e-jN_s\|$	$vjN_s/(kP_e-jN_s)$

in Table 1. The air-gap flux density harmonics with $j = 0$ are stationary. They include the 3rd, 15th, and 21st harmonics produced by PM, as well as the 3rd, 9th, 15th, and 21st harmonics produced by the EC. They yield dc component of the flux linkage, which have no contribution to back-EMF. The air-gap flux density harmonics with $j = 1$ represent the harmonics produced with the modulation of 1st permeance harmonics of secondary core. They are 2nd, 4th, 14th, 20th harmonics produced by PM excitation and 2nd, 4th, 8th, 14th, 20th harmonics produced by EC excitation. They are moving harmonics, yielding the ac component of flux linkage and contributing back-EMF.

3.4. Flux Linkage

A flux linkage calculation model can be established based on the air-gap flux density distribution. It should be particularly noted that the calculation of the flux linkage generated by the EC must account for the influence of the leakage flux (ψ_{el}). Fig. 9 presents a simplified magnetic circuit model of the leakage flux paths, and numbers 1 and 2 represent the coil sides of different phases.

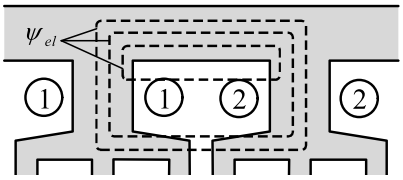

FIGURE 9. Simplified leakage flux paths produced by EC.

According to (7) and (8), the open-circuit flux linkages produced by the PM and EC excitation modes can be expressed as

$$\begin{cases}\psi_m(t) = N_c L_{stk} \int_{x_1}^{x_2} B_m(x,t)dx = \psi_m^{dc} + \psi_m^{ac} \\ \psi_e(t) = N_c L_{stk} \int_{x_1}^{x_2} B_e(x,t)dx + \psi_{el} = \psi_e^{dc} + \psi_e^{ac}\end{cases} \tag{10}$$

where x_1 and x_2 are the initial and end positions of the solution subphase respectively; L_{stk} is the stacking length; ψ_m^{dc} and ψ_m^{ac} represent the dc and ac components of the PM flux linkage, respectively; ψ_e^{dc} and ψ_e^{ac} represent the dc and ac components of the EC flux linkage, respectively.

As derived from (9), the stationary air-gap flux density harmonics and ψ_{el}, which are not generated by the air-gap flux density, contribute to the dc component of the flux linkage, whereas the moving air-gap flux density harmonics with orders of $|iP_m \pm jN_s|$ and $|kP_e \pm jN_s|$ generate the ac component of the flux linkage. Furthermore, these harmonics with $j = 1$ generate the fundamental component of the flux linkage.

Figure 10 shows the amplitudes of both the dc and fundamental components of the flux linkage calculated using the semi-analytical and FEA methods. The semi-analytical method refers to using (9) and the amplitudes of the air-gap flux density harmonics calculated from the FEA solutions for an accurate harmonic analysis. As shown, excellent agreement was achieved, confirming the validity of the analytical flux linkage formulation.

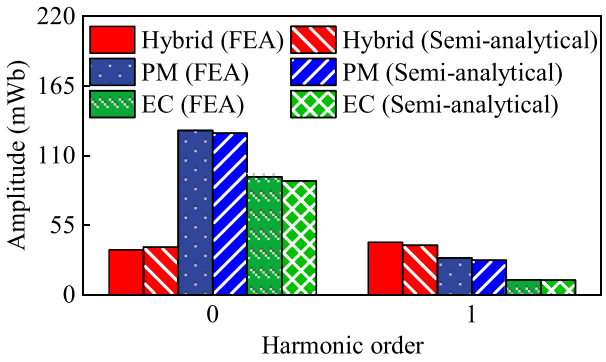

FIGURE 10. Comparison of subphase flux linkage harmonics between semi-analytical and FEA method.

As shown in Fig. 10, compared with PM excitation, the hybrid excitation achieves a 72.4% reduction in the dc component of the flux linkage, which effectively relieves the magnetic saturation in the primary iron core. Meanwhile, the fundamental component increased by 41.5%, thereby enhancing both the back-EMF and thrust force.

The contributions of the stationary air-gap flux density harmonics, that is, groups 1 and 4 in Table 1, to the dc component of the flux linkage are summarized in Fig. 11. The analysis revealed that the 3rd harmonic exerted the most significant influence. This dominance stems not only from the highest amplitude among all harmonics in the air-gap flux density but also from the lowest harmonic order. Notably, the dc components of the flux linkages by the 3rd air-gap flux density harmonics under PM and EC excitations exhibit opposite polarities and weaken each other. Additionally, the polarity of ψ_{el} is identical to the EC flux, thereby further decreasing the dc component of the flux linkage produced by the PM. Overall, the introduction of the EC led to a reduction in the dc component of the flux linkage under hybrid excitation.

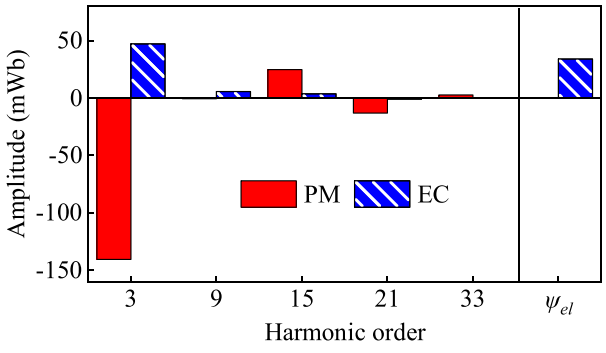

FIGURE 11. The dc component of the open circuit flux linkage contributed by the air-gap flux density harmonics and flux leakage under PM and EC excitations.

The contributions of the moving air-gap flux density harmonics, that is, groups 2, 3, 5, and 6 in Table 1, to the fundamental component of flux linkage are summarized in Fig. 12. The results show that the 2nd, 4th, 14th, and 20th harmonics contribute most significantly. The subphases of the flux linkages generated by these air-gap flux density harmonics are either in phase or in 180° phase shift. For example, the 2nd air-gap flux density harmonics generated by PM and EC excitations share identical phase angles, consequently producing in-phase flux linkage. Overall, the fundamental flux linkages generated by both EC and PM excitations enhanced each other. Consequently, the fundamental component of the flux linkage increased under hybrid excitation.

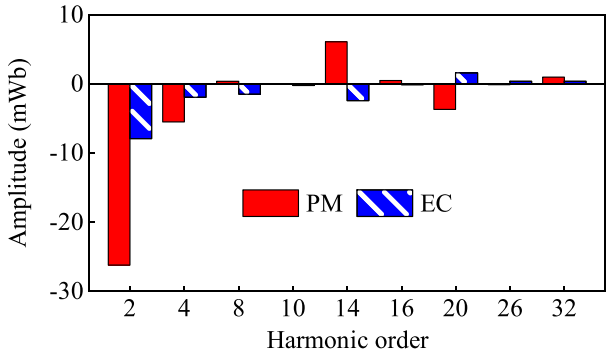

FIGURE 12. The fundamental component of open circuit flux linkage contributed by the air-gap flux density harmonics under PM and EC excitations.

Figure 13 shows the flux linkage waveforms of C1 subphase under various excitation conditions. It can be observed that the waveforms of flux linkage are sinusoidal under all excitation conditions; therefore, the high-order harmonics in the ac components can be negligible. Furthermore, the dc component of the flux linkage under hybrid excitation is significantly re-

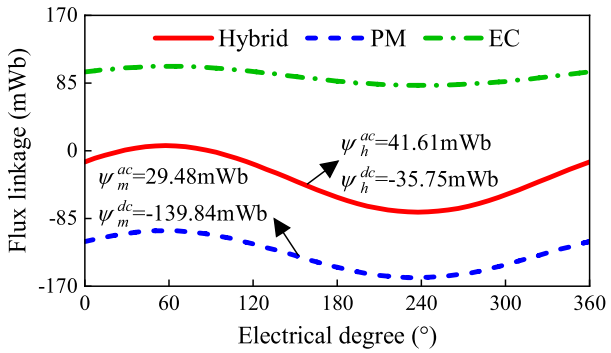

FIGURE 13. Subphase open circuit flux linkage waveforms under different excitations.

duced, which helps to relieve magnetic saturation in the primary iron core. As shown, the amplitude of the ac component of the flux linkage increased from 29.48 mWb under PM excitation to 41.61 mWb under hybrid excitation. In addition, the amplitude of dc component of the flux linkage decreased from 139.84 mWb under PM excitation to 35.75 mWb under hybrid excitation.

The electromagnetic thrust force is generated by the interaction between the hybrid excitation and armature fields. In addition, owing to the negligible reluctance thrust force, the d-axis current, I_d, is set to zero. Therefore, the thrust force expression is

$$F = \frac{6\pi}{\tau_s}(\psi_{m,1} + \psi_{e,1})I_q = \frac{6\pi}{\tau_s}(\psi_{m,1} + \psi_{e,1})I_{ac} \qquad (11)$$

where $\psi_{m,1}$ and $\psi_{e,1}$ are the fundamental amplitudes of flux linkages produced by the PM and EC excitations, respectively. I_q is the q-axis current, and I_{ac} is the amplitude of the AC current component in the integrated winding, which is equal to I_q when $I_d = 0$. It can be observed that the thrust force is proportional to both the EC and armature current.

4. ELECTROMAGNETIC PERFORMANCE ANALYSIS AND COMPARISON

The machine is optimized by using genetic algorithm coupled with FEA. The maximum average thrust force and minimum thrust force ripple are selected as the optimization objectives. The total copper loss produced by both dc and ac currents is fixed to 100 W. Fig. 14 shows the geometric parameters of the proposed FM-HELM.

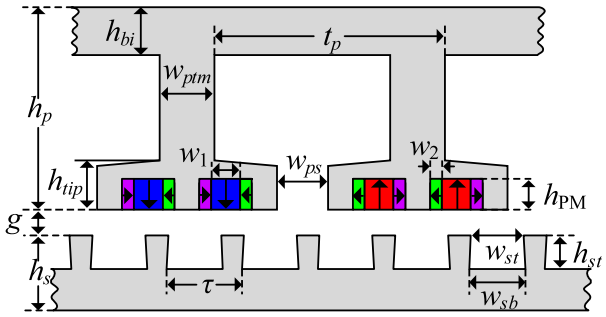

FIGURE 14. Geometric parameters of the proposed FM-HELM.

The constant geometric parameters of the machine are set as follows: The primary pole pitch (t_p) is 49 mm; the primary height (h_p) is 45 mm; the air gap length (g) is 2 mm; the secondary pole pitch (τ_s) is 17.29 mm; the secondary height (h_s) is 18 mm; the stack length (L_{ef}) is 120 mm. In genetic algorithm, the initial population size and number of iterations are set to 100 and 50. Table 2 lists the optimal values of design parameters.

4.1. Flux Regulation Capability

Figure 15 shows the open circuit flux linkages under flux-enhancing, PM, and flux-weakening excitation conditions. The

TABLE 2. Optimal values of design parameters of the proposed FM-HELM.

Symbol	Design Parameters	Unit	Value
h_{PM}	PM height	mm	6.97
w_1	Vertically magnetized PM width	mm	5.55
w_2	Horizontally magnetized PM width	mm	2.52
w_{ps}	Primary slot opining	mm	9.66
w_{ptm}	Primary tooth width	mm	11.65
h_{bi}	Back iron height	mm	8.17
h_{tip}	Tooth height	mm	7.27
w_{st}	Secondary slot width	mm	12.01
w_{sb}		mm	12.80
h_{st} /h_s	Secondary pole height ratio	/	0.45

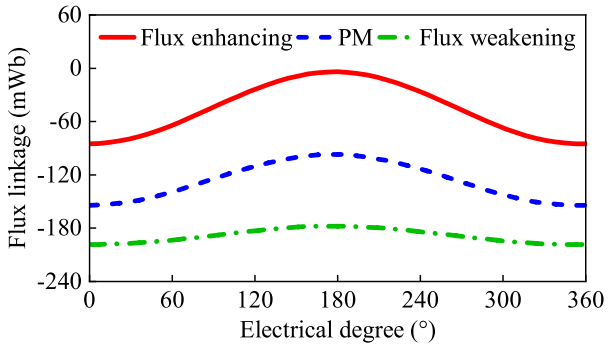

FIGURE 15. Subphase open-circuit flux linkage under flux enhancing, PM and flux weakening excitation conditions.

flux-enhancing and flux-weakening excitation conditions are hybrid excitations, where both PM and EC excitations are involved. The flux-weakening excitation condition has the opposite EC direction to that of the flux-enhancing excitation condition. Compared to the PM and flux-weakening excitation conditions, the amplitude of the dc component of flux linkage under the flux-enhancing excitation condition decreases noticeably. In addition, the ac component of flux linkage under the flux-enhancing excitation condition increased significantly. This contributes to relieving the primary iron core magnetic saturation and improving the flux regulation capability.

Figure 16 presents the open-circuit magnetic field distributions under PM and flux enhancing excitation conditions. It is noted that the primary and secondary iron core magnetic saturation under flux-enhancing excitation conditions is relieved compared to that under PM excitation conditions, which is consistent with the above theoretical analysis.

Figure 17 shows the open-circuit flux linkage under varying DC currents. The DC component of the flux linkage is seen to decrease gradually with increasing DC current. At a DC current of 5 A, this component approaches zero, suggesting that magnetic saturation caused by DC flux linkage in the primary core is almost entirely suppressed.

Figure 18 depicts the open-circuit back-EMF waveforms under flux enhancing, PM, and flux-weakening excitation conditions. Compared with the PM excitation condition, the amplitude of the open-circuit back-EMF significantly increased

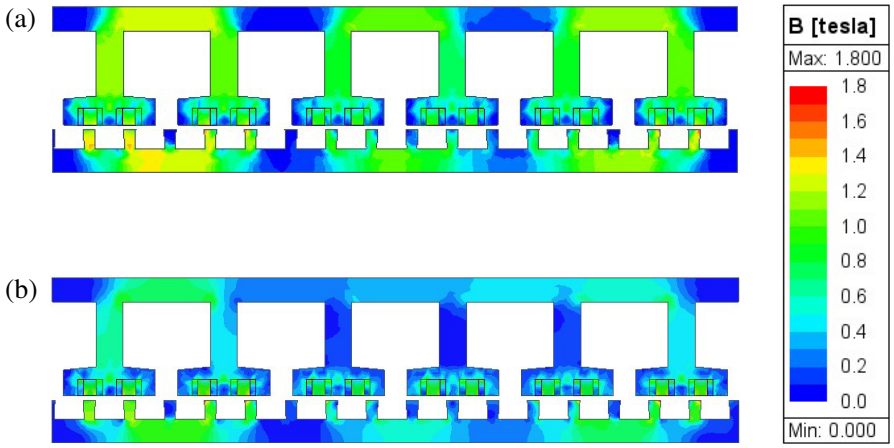

FIGURE 16. Open-circuit magnetic field distribution. (a) PM excitation. (b) Flux-enhancing excitation.

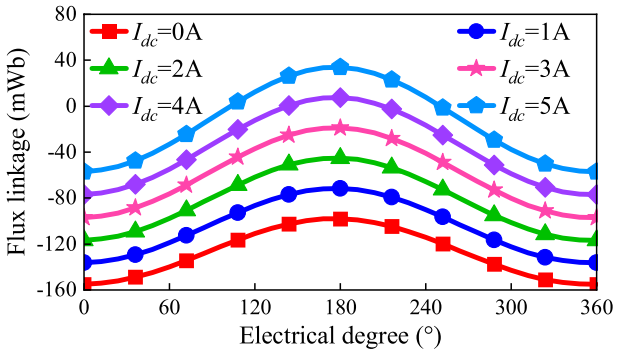

FIGURE 17. Variation characteristics of open circuit flux linkage with different DC currents.

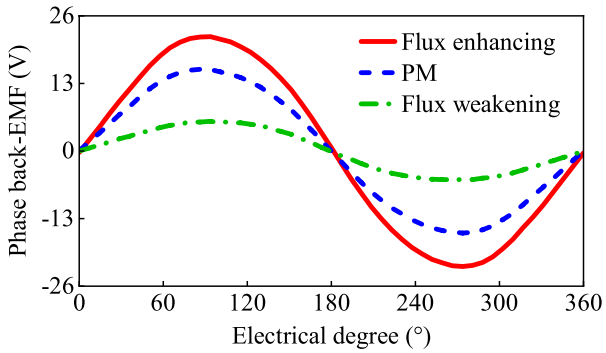

FIGURE 18. Open circuit back-EMF waveforms under flux enhancing, PM and flux weakening excitation conditions.

and decreased under the flux-enhancing excitation condition and flux-weakening excitation conditions, respectively. In addition, the switch between flux-enhancing and flux-weakening excitation conditions can be simply realized by reversing the direction of the DC current in the integrated winding. Furthermore, by adjusting the magnitude of the DC current, an adjustable back-EMF amplitude can be achieved.

Flux regulation capability is a crucial indicator of electromagnetic performance. To quantitatively evaluate this capability, the concept of the flux regulation ratio is defined as

$$k_f = \frac{E_{FE} - E_{FW}}{E_0} \tag{12}$$

where E_{FE}, E_{FW}, and E_0 represent the fundamental amplitudes of the subphase back-EMF under flux-enhancing, flux-weakening, and PM excitation conditions, respectively. Calculations show that E_{FE}, E_{FW}, and E_0 are 21.97, 5.68, and 15.67 V, respectively. This yielded a 104% flux regulation ratio, which confirmed the superior flux regulation capability of the FM-HELM.

4.2. Thrust Force Characteristic

Figure 19 illustrates the variation in the average thrust force with the dc copper loss ratio (k_{dc}). The k_{dc} is defined as

$$\begin{cases} I_{dc} = \sqrt{k_{dc}} I_{rms} \\ I_{ac} = \sqrt{2 - 2k_{dc}} I_{rms} \end{cases} \tag{13}$$

where I_{rms} is the root-mean-square value of the total current in the integrated winding, and I_{dc} and I_{ac} are the amplitudes of the dc and ac components of the current in the integrated winding, respectively.

The results demonstrate that for any given copper loss, an optimal k_{dc} exists that maximizes the average thrust force. Notably, the average thrust force was large and exhibited minimal variation when the k_{dc} is below 0.4. Subsequently, the average thrust force showed an obvious decline as the proportion of the DC current increased. As can be seen, under the condition of 100 W copper loss (3.6 A/mm^2), the FM-HELM achieves a 24.84% improvement in average thrust force compared with PM excitation ($k_{dc} = 0$).

Figure 20 illustrates the variation in the average thrust force under flux-enhancing and PM excitation conditions. It can be observed that under the same copper loss conditions, compared to PM excitation, the FM-HELM in the flux enhancing excitation exhibits a 24.84% increase in average thrust force and a

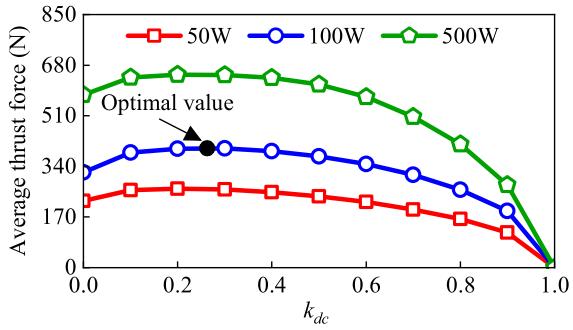

FIGURE 19. Variation of average thrust force with dc copper loss ratio k_{dc}.

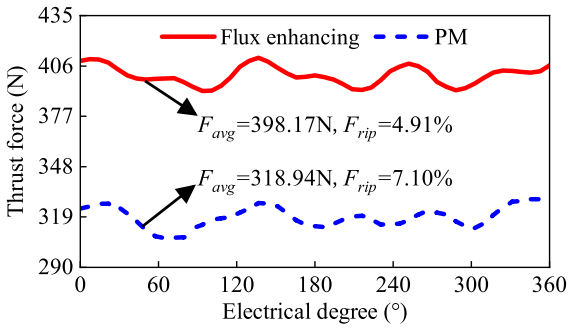

FIGURE 20. Thrust force comparison of flux enhancing and PM excitation conditions under rated copper loss (100 W).

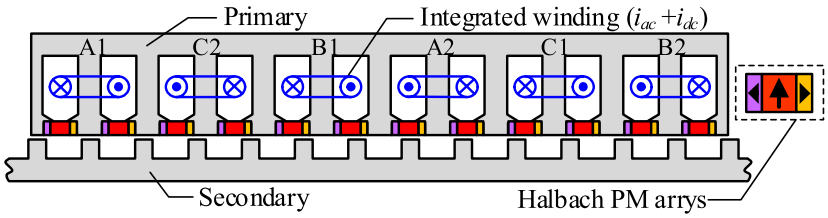

FIGURE 21. Topology of the existing FM-HELM.

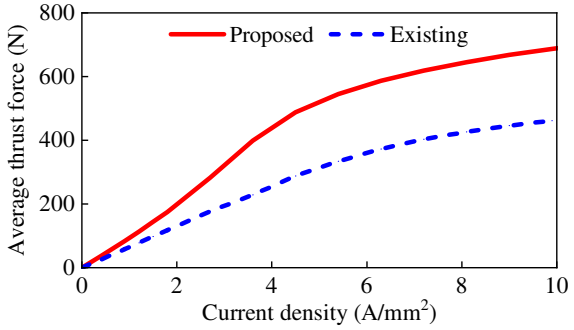

FIGURE 22. Average thrust force comparison of the proposed and existing machines with different current density.

30.84% reduction in thrust ripple. This indicates that a significant overall improvement in the thrust force performance was achieved under flux enhancing conditions.

To assess the electromagnetic performance of the proposed machine, it was compared with an existing optimal FM-HELM with the same machine size [19]. The topology of existing FM-HELM is illustrated in Fig. 21.

Figure 22 shows the average thrust force characteristics of the existing and proposed FM-HELMs with different current densities. The proposed machine exhibits a higher average thrust force than its counterpart under all conditions, that is, small, moderate, and high current densities. In addition, the improvement in the average thrust force is more pronounced under high current density conditions, which is attributed to the anti-saturation characteristic of the proposed FM-HELM.

Table 3 shows a detailed comparison of the two machines under copper losses of 100 W. Overall, the proposed machine offers superior thrust force performance, i.e., higher average thrust force and lower force ripple. Also, the flux regulation capability of the proposed machine is much higher than that

TABLE 3. Performance comparison of two machines.

Performance	Proposed	Existing
Average thrust force (N)	398.14	229.08
Force ripple (%)	4.38	20.13
Flux regulation ratio (%)	104%	32%
Copper loss (W)	100	100
Iron loss (W)	31.3	18.6
PM eddy current loss (mW)	311.6	464.23
Efficiency (%)	81.90	74.27

of the existing one. Both machines have negligible PM eddy current loss as compared to their iron loss and copper loss. In spite of higher iron loss in the proposed machine, it offers higher efficiency due to its higher thrust force output.

5. CONCLUSION

In this study, an FM-HELM suitable for long-stroke linear applications is proposed. The integrated winding avoids the problem of winding space contradiction and improves the utilization rate of the winding. The EC in the integrated winding not only relieves the magnetic saturation in the primary iron core but also generates working air-gap flux density harmonics. Thus, improved thrust force and flux regulation capability are achieved. Based on the flux modulation theory, the MMF permeance model is used to deduce the air-gap flux density under hybrid excitation, and the mechanism of relieving magnetic saturation is further revealed. The flux regulation capability and thrust force characteristics were analyzed using FEA. Compared with the case of PM excitation only, the average thrust force of hybrid excitation can be effectively increased. In addition, it offers good overload capacity and flux regulation capability.

REFERENCES

[1] Boldea, I., L. N. Tutelea, W. Xu, and M. Pucci, "Linear electric machines, drives, and maglevs: An overview," *IEEE Transactions on Industrial Electronics*, Vol. 65, No. 9, 7504–7515, Sep. 2018.

[2] Eckert, P. R., A. F. F. Filho, E. A. Perondi, and D. G. Dorrell, "Dual quasi-halbach linear tubular actuator with coreless moving-coil for semiactive and active suspension," *IEEE Transactions on Industrial Electronics*, Vol. 65, No. 12, 9873–9883, Dec. 2018.

[3] Cao, R., Y. Jin, M. Lu, and Z. Zhang, "Quantitative comparison of linear flux-switching permanent magnet motor with linear induction motor for electromagnetic launch system," *IEEE Transactions on Industrial Electronics*, Vol. 65, No. 9, 7569–7578, Sep. 2018.

[4] Li, Z. and S. Niu, "Overview of variable flux reluctance linear machines for long-stroke applications," *IEEE Transactions on Transportation Electrification*, Vol. 11, No. 1, 448–462, Feb. 2025.

[5] Gao, Y., Y. Lyu, H. Huang, and R. Qu, "Review of flux modulation linear permanent magnet machines," *IEEE Transactions on Transportation Electrification*, Vol. 11, No. 1, 2629–2647, Feb. 2025.

[6] Zhu, Z. Q., X. Chen, J. T. Chen, D. Howe, and J. S. Dai, "Novel linear flux-switching permanent magnet machines," in *2008 International Conference on Electrical Machines and Systems*, 2948–2953, Wuhan, China, 2008.

[7] Cao, R., M. Lu, N. Jiang, and M. Cheng, "Comparison between linear induction motor and linear flux-switching permanent-magnet motor for railway transportation," *IEEE Transactions on Industrial Electronics*, Vol. 66, No. 12, 9394–9405, Dec. 2019.

[8] Cao, R., Y. Jin, Z. Zhang, and M. Cheng, "A new double-sided linear flux-switching permanent magnet motor with yokeless mover for electromagnetic launch system," *IEEE Transactions on Energy Conversion*, Vol. 34, No. 2, 680–690, Jun. 2019.

[9] Zhang, Z., X. Tang, C. Zhang, and M. Li, "Novel decoupling modular permanent magnet flux-switching linear motor," *IEEE Transactions on Industrial Electronics*, Vol. 66, No. 10, 7603–7612, Oct. 2019.

[10] Boldea, I., C. Wang, B. Yang, and S. A. Nasar, "Analysis and design of flux-reversal linear permanent magnet oscillating machine," in *Conference Record of 1998 IEEE Industry Applications Conference. Thirty-Third IAS Annual Meeting (Cat. No.98CH36242)*, Vol. 1, 136–143, St. Louis, MO, USA, 1998.

[11] Kou, B., J. Luo, X. Yang, and L. Zhang, "Modeling and analysis of a novel transverse-flux flux-reversal linear motor for long-stroke application," *IEEE Transactions on Industrial Electronics*, Vol. 63, No. 10, 6238–6248, Oct. 2016.

[12] Liu, G., H. Zhong, L. Xu, and W. Zhao, "Analysis and evaluation of a linear primary permanent magnet vernier machine with multiharmonics," *IEEE Transactions on Industrial Electronics*, Vol. 68, No. 3, 1982–1993, Mar. 2021.

[13] Ullah, B., F. Khan, S. Hussain, and B. Khan, "Modeling, optimization, and analysis of segmented stator flux switching linear hybrid excited machine for electric power train," *IEEE Transactions on Transportation Electrification*, Vol. 8, No. 3, 3546–3553, Sep. 2022.

[14] Zeng, Z., Y. Shen, Q. Lu, B. Wu, D. Gerada, and C. Gerada, "Investigation of a partitioned-primary hybrid-excited flux-switching linear machine with dual-PM," *IEEE Transactions on Industry Applications*, Vol. 55, No. 4, 3649–3659, Jul.–Aug. 2019.

[15] Zhu, Z. Q. and B. Lee, "Integrated field and armature current control for dual three-phase variable flux reluctance machine drives," *IEEE Transactions on Energy Conversion*, Vol. 32, No. 2, 447–457, Jun. 2017.

[16] Shen, Y., Q. Lu, T. Shi, and C. Xia, "Analysis and evaluation of hybrid-excited doubly salient permanent magnet linear machine with dc-biased armature current," *IEEE Transactions on Industry Applications*, Vol. 57, No. 4, 3666–3677, Jul.–Aug. 2021.

[17] Shen, Y. and Q. Lu, "Design and analysis of hybrid-excited flux modulated linear machines with zero-sequence current excitation," *IEEE Journal of Emerging and Selected Topics in Power Electronics*, Vol. 10, No. 2, 1834–1846, Apr. 2022.

[18] Li, Z., F. Ni, S. Niu, and K. T. Chau, "Novel zero-sequence current excited double-sided vernier reluctance linear machine with high-order-harmonic toroidal winding," *IEEE Transactions on Magnetics*, Vol. 61, No. 9, 1–6, Sep. 2025.

[19] Shen, Y., Q. Lu, and Y. Li, "Design criterion and analysis of hybrid-excited vernier reluctance linear machine with slot Halbach PM arrays," *IEEE Transactions on Industrial Electronics*, Vol. 70, No. 5, 5074–5084, 2023.